sustainability

MDPI

Article

A Seismic Monitoring Tool for Tidal-Forced Aquifer Level Changes in the Río de la Plata Coastal Plain, Argentina

Luciano Galone [1,*], Francesco Panzera [2], Emanuele Colica [1,3], Enrique Fucks [4,5], Eleonora Carol [4,6], Francisco Cellone [4,7], Lluís Rivero [8,9], Matthew R. Agius [1] and Sebastiano D'Amico [1]

1 Department of Geosciences, University of Malta, MSD 2080 Msida, Malta; emanuele.colica@um.edu.mt (E.C.); matthew.agius@um.edu.mt (M.R.A.); sebastiano.damico@um.edu.mt (S.D.)
2 Biological, Geological and Environmental Sciences Department, University of Catania, 95129 Catania, Italy; francesco.panzera@unict.it
3 Research and Planning Unit, Public Works Department, Ministry for Public Works and Planning, FRN 1700 Floriana, Malta
4 Facultad de Ciencias Naturales y Museo, National University of La Plata, La Plata 1900, Argentina; efucks@fcnym.unlp.edu.ar (E.F.); eleocarol@fcnym.unlp.edu.ar (E.C.); fcellone@fcnym.unlp.edu.ar (F.C.)
5 Centro de Estudios Integrales de la Dinámica Exógena, National University of La Plata (CEIDE-CIC-UNLP), La Plata 1900, Argentina
6 Centro de Investigaciones Geológicas, Consejo Nacional de Investigaciones Científicas y Técnicas, National University of La Plata (CIG-CONICET-UNLP), La Plata 1900, Argentina
7 Centro de Investigaciones del Medio Ambiente, Consejo Nacional de Investigaciones Científicas y Técnicas, National University of La Plata (CIM-CONICET-UNLP), La Plata 1900, Argentina
8 Mineralogy, Petrology and Applied Geology, Universitat de Barcelona, 08028 Barcelona, Spain; lrivero@ub.edu
9 Water Research Institute, Universitat de Barcelona, 08001 Barcelona, Spain
* Correspondence: luciano.galone@um.edu.mt

Abstract: Ambient seismic noise has gained extensive applications in seismology and plays a pivotal role in environmental seismic studies. This study focuses on the Río de la Plata Coastal Plain, employing the horizontal-to-vertical spectral ratio (HVSR) method on ambient seismic noise records to analyze subsurface dynamics. The region's hydrogeology is complex, featuring partially interconnected coastal aquifers. The HVSR analysis reveals two peaks, with P_0 associated with the sediment-basement interface and P_1 linked to a shallower stratigraphic discontinuity. Temporal analysis of P_1 highlights cyclical patterns correlated with estuarine levels, suggesting a relationship between variations in seismic velocities and tidal dynamics. Comparisons with aquifer data support the hypothesis that tidal variations influence subsurface mechanical properties, impacting the HVSR function. The study hints at the potential of ambient seismic noise analysis as a non-invasive and cost-effective method for studying coastal aquifers and understanding groundwater dynamics. Ongoing research aims to further explore these relationships for enhanced groundwater resource management.

Keywords: ambient seismic noise; aquifer level; horizontal-to-vertical spectral ratio variability

Citation: Galone, L.; Panzera, F.; Colica, E.; Fucks, E.; Carol, E.; Cellone, F.; Rivero, L.; Agius, M.R.; D'Amico, S. A Seismic Monitoring Tool for Tidal-Forced Aquifer Level Changes in the Río de la Plata Coastal Plain, Argentina. *Sustainability* **2024**, *16*, 1432. https://doi.org/10.3390/su16041432

Academic Editor: Antonio Miguel Martínez-Graña

Received: 30 November 2023
Revised: 31 January 2024
Accepted: 4 February 2024
Published: 8 February 2024

1. Introduction

Effective water management plays a crucial role in promoting sustainable development by addressing the responsible use of this vital resource (e.g., [1,2]). In this context, the study of aquifers presents unique challenges due to their subsurface location, requiring diverse approaches to their characterization and management. Several methods have been developed to address this complexity that are both direct and indirect (e.g., [3–5]). Groundwater management involves a global perspective that encompasses various aspects. Given the importance and complexity of these reservoirs, it is imperative to continue perfecting advanced techniques for their study and proper management.

Ambient seismic noise has gained extensive applications in the frame of seismology, proving to be valid in examining diverse environments across varying scales. Ambient

seismic noise comprises body and surface waves spanning a broad frequency spectrum from microseismic activity (<0.1 Hz) to higher-frequency noise attributed to anthropogenic factors (>10 Hz). The origins of ambient vibrations can be linked to both natural sources, including earthquakes, volcanoes, storms, and geothermal activities, and anthropogenic sources, such as factories, traffic, and engines. These vibrations find practical utility in various applications, such as local or regional passive seismic tomography [6,7] and engineering seismology aimed at understanding seismic site effects [8–10]. Additionally, they play a pivotal role in environmental seismology applications, monitoring parameters such as aquifer levels [11,12], river transportation characteristics [13,14], glacier discharge [15,16], landslides [17–19], and meteo-marine events associated with phenomena like "hurricane" and "microseism" [20,21]. A key advantage of ambient vibrations lies in their continuous nature, offering an uninterrupted signal capable of capturing alterations in the subsoil's physical properties. This characteristic enables simultaneous recording at multiple locations. Leveraging this advantage, techniques can be implemented to monitor signals emanating from natural features such as seas, glaciers and rivers, providing insights into their current status and evolving physical attributes.

Most of the aforementioned methods are based on the analysis of Fourier spectra content of the ambient vibrations, but especially in engineering seismology, ambient seismic noise is often processed using the horizontal-to-vertical spectral ratio (HVSR) method [22,23]. The HVSR method is valid for obtaining information on the fundamental frequency of the investigated site, which is related to the main velocity contrast at depth. The method is applied successfully in several contexts, although the obtained spectral ratio amplitudes cannot be related to the real amplification (e.g., [24–28]).

In the last few years, some works have documented changes through time in the HVSR shape. The ambient vibrations wavefield is composed of a time-dependent percentage of body waves and surface waves that travel within the upper layers of the Earth's crust and changes in the percentages of each wave component [29,30]. A possible explanation for the HVSR shape amplitude variation can be ascribed to the ambient vibration wavefield composition, which is variable in time [31–35]. The change in seismic wave velocity affects the propagation of seismic waves [36,37] with consequences for the HVSR shape [31,35]. The reasons for these shear wave velocity variations can be related to the change in pore pressure due to the oscillations of the water tables and the seasonal distribution of precipitation on soil, with a shear wave velocity (V_S) that drops in the overpressure zone [38,39]. Recent experimental studies have linked temporal changes in the HVSR function to variations within the active layer of permafrost [40] or fluctuations in groundwater levels [41,42].

Despite the growing utilization of HVSR on ambient seismic noise records, there exists a significant gap in the understanding of HVSR variations over time, especially in coastal regions impacted by tidal fluctuations, which have received limited attention in previous studies. This paper seeks to address this gap by investigating the relationship between HVSR records, tidal variations and the hydrogeology of the Rio de la Plata Coastal Plain. It is a domain of great importance due to its environmental value as a wetland habitat and as a support for coastal communities. To achieve this purpose, we used ambient seismic noise recordings collected at a temporary seismic station set up specifically for this study. These data were processed using the HVSR technique, and the results were examined in relation to the local stratigraphy. Subsequently, we explored the temporal changes in the HVSR function and compared them with the tidal fluctuations observed in the Río de la Plata. By analyzing the interaction between the unconfined aquifer, a semi-confined aquifer, and the tides, we hypothesize a conceptual model that explains the experimentally obtained HVSR results.

2. The Río de la Plata Coastal Plain

The Río de la Plata, located on the western coast of the South Atlantic at approximately 35–36° S, is an extensive and shallow estuary (Figure 1). Its significance lies in the fact that it receives freshwater inflow from the second-largest basin in South America, covering an

area of approximately 3.2 million Km^2 [43]. With a funnel-like shape, the Río de la Plata estuary extends for over 280 Km from its head, where it is approximately 25 Km wide, formed by the convergence of the Paraná and Uruguay rivers, to its mouth, which widens to approximately 230 Km. It forms an estuarine system spanning around 35,000 Km^2, characterized by relatively shallow waters ranging from 5 to 15 m in depth. The estuary operates with a semidiurnal and micro-tidal pattern, and the water salinity levels vary from around 2 g/L in the inner and middle sections to around 20 g/L in the outer section [44,45].

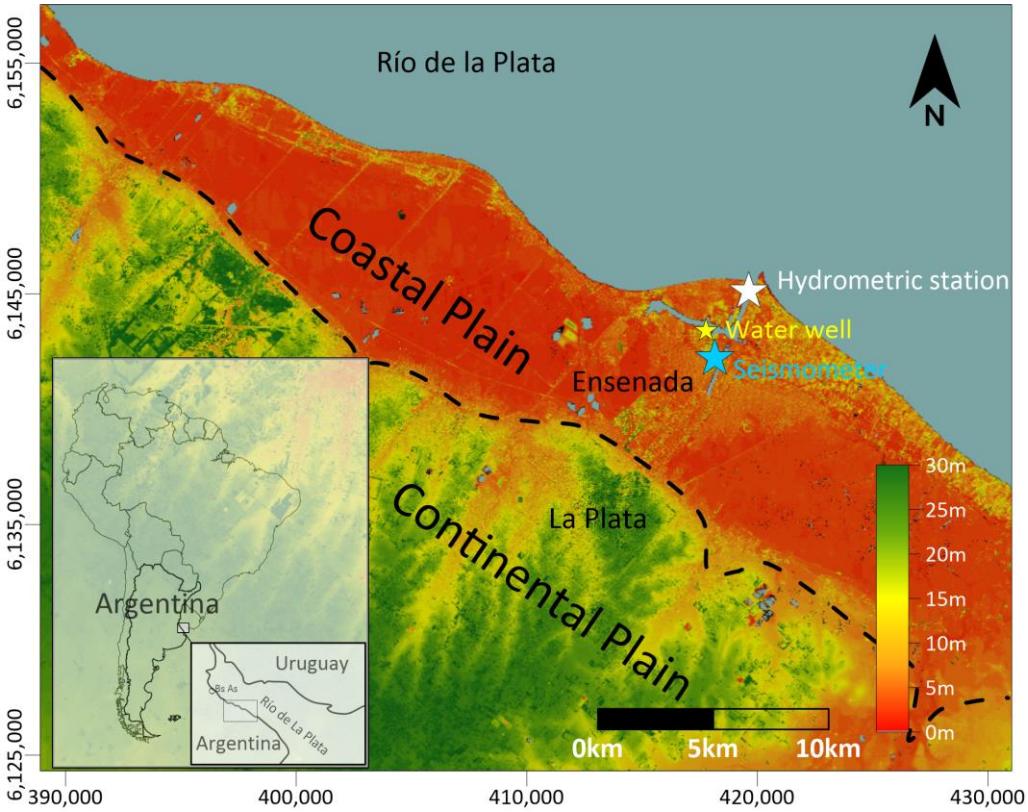

Figure 1. Topographic map showing the coastal plain, at altitudes below 5 m asl, the continental plain, and their position in South America and the in the Río de la Plata. The black dashed line delimits both geomorphologic domains and represents the paleo-scarp. The blue star represents the location of the seismometer installation site. The white star represents the location of the hydrometric station. The smaller yellow star represents the position of the water well data. Coordinates are in UTM- WGS84. Topography source: MDE-Ar (Instituto Geográfico Nacional, Argentina).

The coastal plain on the right bank of the Río de la Plata estuary, extending from the coast to the paleo-scarp that separates it from the continental plain, spans approximately 4 to 8 Km in width and runs parallel to the shoreline. This area has a flat to flat-concave topography, which has led to the development of chaotic drainage networks and extensive floodable wetlands [46,47]. Currently, several artificial canals traverse the area, which were constructed for drainage purposes.

The coastal plain is composed mainly of clayey silt sediments deposited during the Holocene that have an average thickness of less than 10 m, known collectively as post-Pampean sediments [48,49]. These deposits overlie the silt loess deposits of the Pampeano Formation (with around 20 m thickness in the study area) with maximum thicknesses near the estuary and disappearing in the continental plain (Figure 1).

From a hydrogeological perspective, the area exhibits a certain degree of complexity, hosting a series of partially interconnected coastal aquifers. The Pampeano Formation and post-Pampeano sediments together house an unconfined and shallow aquifer (<2 m depth) with thicknesses of approximately 25 m in the study area [50]. The recharge of the

unconfined aquifer is from the infiltration of rainwater and it is estimated that about 20% of the annual precipitation (1060 mm) can infiltrate and recharge the aquifer. The shallow groundwater discharges into streams and depressed areas, and the regional groundwater flow is toward the Río de la Plata [51,52]. Additionally, in coastal sectors during high tides, the aquifer may receive inputs from the estuary [53,54].

Beneath the loessic deposits lies the Puelches Formation (around 32 m thickness in the study area), composed of quartz sand deposits, hosting the Puelche aquifer (around 30 m thickness in the study area). This aquifer is the most important in the region due to exploitation flows and its chemical quality; however, it is mainly used for human and industrial supply in the continental plain area, because the coastal plain area tends to become salinized [51]. The Puelche aquifer is separated from the unconfined aquifer by a thin silt–clay layer, imparting a semiconfined character. Below the Puelches Formation, the Paraná Formation of marine origin developed, which presents clays on top that confine the underlying sandy aquifer.

3. Materials and Methods

From 19 to 24 October 2023, we acquired 106 h of ambient seismic noise using a portable triaxial digital seismograph (Geobit instruments) on the outskirts of the city of Ensenada, Argentina, which was temporarily installed for that purpose (Figure 1). The device was positioned on the coastal plain of the Río de la Plata, close to estuary-linked channels with water levels that fluctuate in sync with the estuary's tidal variations. The coast of the estuary was about 3.5 Km away in a straight line. The equipment was installed directly on the natural soil, levelled, and oriented towards the geographical north. Data were acquired with a sampling rate of 200 Hz. The data were synchronized through the use of a global positioning system (GPS).

Data were later processed using Geopsy version 3.4.2, an open-source software for organizing, visualizing and processing geophysical signals [55]. The signals were processed using the HVSR technique [22,29,56,57]. This technique is based on dividing the spectrum of each of the three components into time windows of a selected time-series duration, which in our case was 40 s. We also performed tests with longer time windows of up to 3600 s; however, the differences were insignificant ($\leq$5%). A relative threshold of 10% was applied to eliminate possible erroneous samples. The Fourier amplitude spectra of each time window were then calculated and smoothed. The horizontal spectrum was obtained by quadratically averaging both horizontal components. The averaged HVSR curve was calculated using the HVSR curves of each time window and applying the smoothing method of [58]. The signals were analyzed in the frequency range from 0.1 to 10 Hz. The frequency peak and its associated standard deviation were calculated by averaging the maximum frequency found in the HVSR curve for each time window within a 10% interval around the peak of the averaged HVSR curve [55]. Using the same parameters, we calculated the spectrum for each of the two horizontal components and the vertical component.

4. Results

The HVSR curve obtained for the entire recording is well-defined, with relatively low standard deviations at frequencies above 0.5 Hz. At lower frequencies, the standard deviations increase as frequencies decrease, especially below 0.3 Hz, although they remain in an acceptable range. The HVSR curve obtained shows two clear peaks: one at low frequencies, which we refer to as P_0, and another at higher frequencies, which we refer to as P_1 (Figure 2).

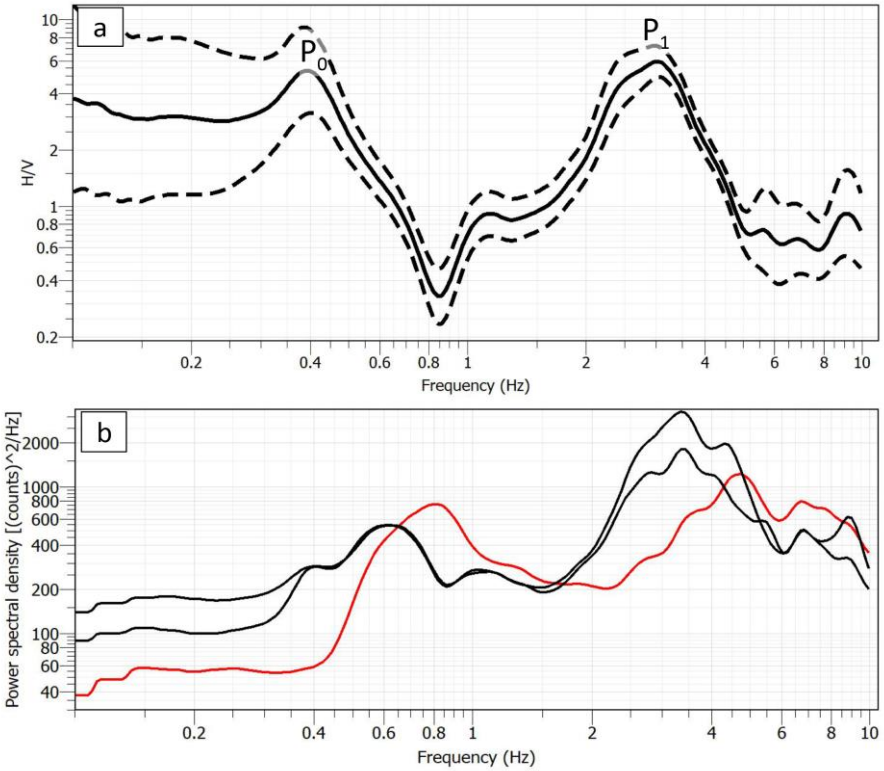

Figure 2. HVSR obtained for the entire recording. Panel (**a**) shows the average HVSR curve (continuous black line) and its standard deviation (dashed black lines). In the plot are indicated the P_0 and P_1 peaks. Panel (**b**) shows the Fourier spectra of the individual components, where the red line represents the vertical component and the black lines represent the horizontal components.

P_0 has a mean value of 0.38 Hz, and it ranges between 0.33 and 0.43 Hz. The HVSR amplitude is 5.27, with values ranging between 2.75 and 10.11, considering a standard deviation. At lower frequencies, the HVSR function stabilizes around 4 units, with higher variabilities evidenced by an enlargement of the area between the dashed lines. At higher frequencies, the function drops around 0.85 Hz, reaching HVSR minimum values close to 0.35 units.

P_1 presents a mean frequency of 2.91 Hz, with frequencies ranging from 2.64 to 3.19 Hz with one standard deviation. The amplitude of the peak has a mean value of 5.81 HVSR units, ranging from 4.5 to 7.42 HVSR units. Similar to P_0, the low-frequency flank of the peak shows slightly higher variabilities than the high-frequency flank. After the peak, towards higher frequencies, the function drops to values close to 0.80 units.

In the extensive HVSR literature, it is widely accepted that HVSR peak frequencies can originate from subsurface geologic discontinuities associated with a Vs contrast (e.g., [59,60]). The simplest case of an HVSR curve with a single peak is usually interpreted as a sedimentary column where relatively low Vs sediments rest on a relatively high Vs bedrock. Curves with more than one peak are usually interpreted as more than one Vs discontinuity, commonly linked to geology. The lower-frequency peak originates from the deepest discontinuity, usually linked to the bedrock, and the higher-frequency peaks correspond to shallower structures.

Using the same parameters to process HVSR, we analyzed the average simple-component Fourier spectra. Both horizontal components showed a similar behavior, while the vertical component exhibited a similar pattern with a variable shift towards higher frequencies. This generated two "eye-shaped patterns" enveloped by the horizontal components above and the vertical one below, corresponding with the frequencies of the P_0 and P_1 peaks. Such a geometry of the spectral components is typical of peaks related to impedance contrasts of stratigraphic origin and constitutes a key validation criterion in geological studies [61].

The underground geology of the study site is known from a borehole in the vicinity of the city of La Plata (Figure 1). At this borehole, the metamorphic basement, known as the Martín García complex, was reached at −467 m beneath sea level (BSL). Overlying the basement are almost 500 m of sedimentary formations, characterized by clastic deposits composed of gravels, sands, silts, and clays. In this context, P_0 likely corresponds to the contact between the rocky basement and the sedimentary column. As for P_1, the higher frequencies suggest an origin associated with a shallower discontinuity within the sedimentary column. This interpretation aligns with previous works dealing with a large HVSR survey conducted in the area [62].

HVSR Time Variations

To check the HVSR peaks variability both in frequency and amplitude we plotted the HVSR function as a function of time for the frequency ranges of 0.2–1 Hz and 1–10 Hz, to preliminarily visualize its behavior. We plotted the single HVSR with respect to time (x-axis), frequency (y-axis) and amplitude in color scale (Figure 3). The results show some variations over time at the P_0 peak (around 0.38 Hz) but with no clear trend. Instead, we recognize a cyclic variation of the HVSR amplitude at the peak frequency P_1 (around 2.91 Hz).

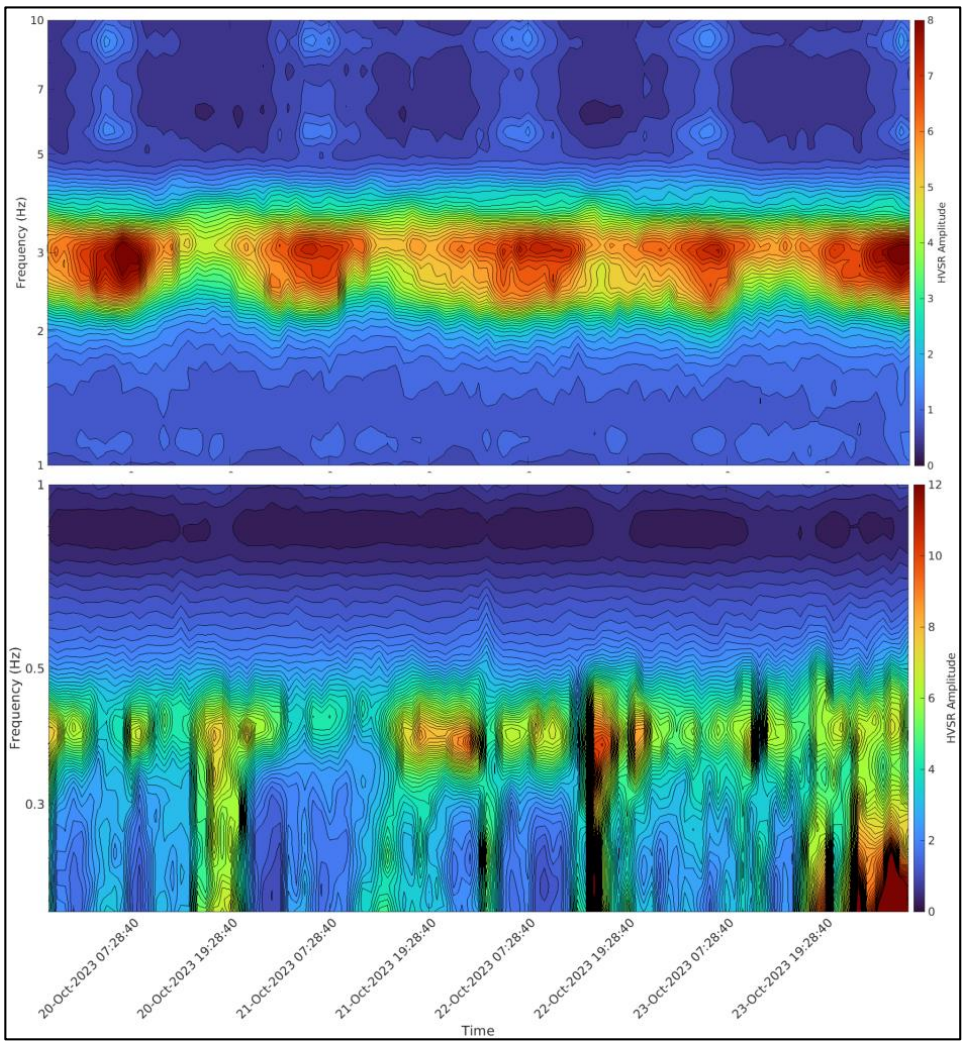

Figure 3. HVSR plot over time for the frequency ranges of 0.2–1.0 Hz (bottom layer) and 1–10 Hz (top layer). Time is reported on the x-axis accordingly with ambient noise measurement records, and on the y-axis, the frequency and the color scale indicate the intensity of the HVSR amplitude.

To further investigate the variability of the HVSR function over time, we calculated the HVSR function for one-hour intervals for the entire recording. During this process, we obtained both the mean frequency value and the HVSR amplitude value for the P_0 and P_1 peaks. In addition, values associated with the standard deviation were included to capture the degree of variability of the data. Results are displayed in x–y plots, with frequencies and HVSR amplitude values on the vertical axis and time on the horizontal axis. To ensure accurate association with time, the midpoint of each hour, at 30 min, is used as a temporal reference in the display of the results (Figure 4).

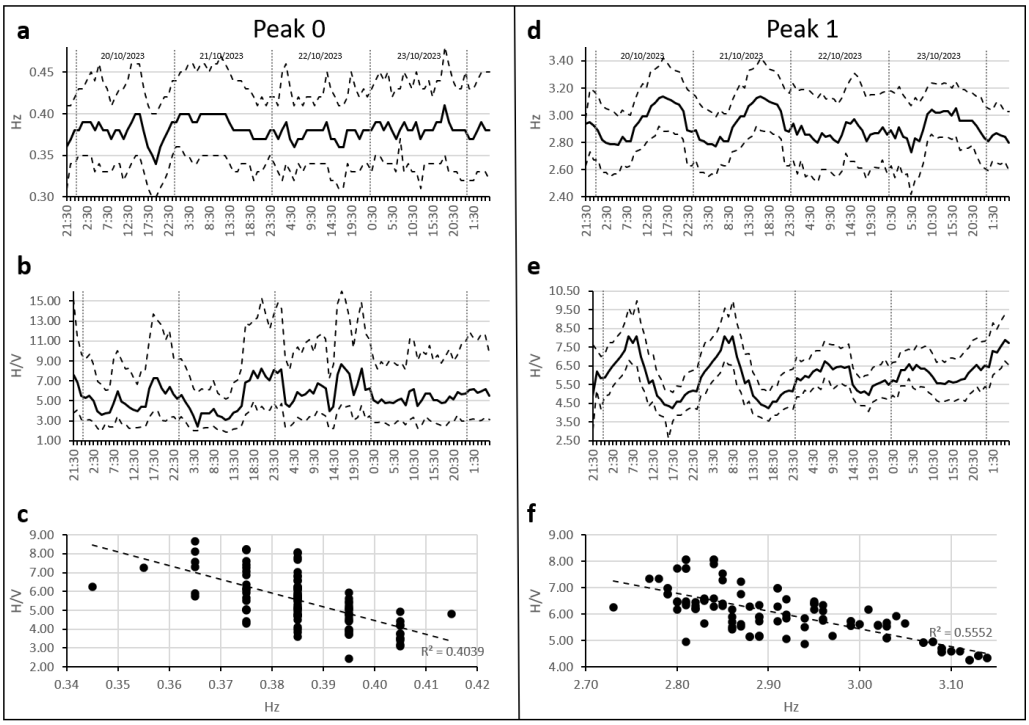

Figure 4. Hourly analysis of P_0, in the left column, and P_1, in the right column. (**a**,**d**) The variation of the frequency of each peak during the recording time. (**b**,**e**) The variation of the HVSR amplitude of each peak over time. The solid line denotes the variation of the mean value, while the dashed lines spanning one standard deviation from the mean. (**c**,**f**) The peak frequency vs. amplitude values, the linear correlation, and the R-squared coefficient.

For P_0 (Figure 4a), we observed a variation in the average frequency values ranging from 0.41 Hz to 0.34 Hz, with a maximum difference of 0.07 Hz, suggesting a relatively low variability in frequencies. In the case of the HVSR amplitude values for P_0, they exhibit a more pronounced variability (Figure 4b). The mean curve reveals maximum values of 8.66 and a minimum of 2.43 for the HVSR, resulting in a range of 6.23 units.

Although the frequency curve shows relatively low variability, there is an apparent correspondence between lower-frequency values and higher HVSR values, and vice versa. A dispersion analysis revealed this trend, and its linear regression exhibits an R-squared coefficient of 0.4039 and a negative slope (Figure 4c). This suggests an inverse relationship between frequencies and HVSR values for P_0.

On the other hand, P_1 hourly analysis has demonstrated a temporal variability of a range of 0.41 Hz, with maxima values of 3.14 Hz and minima values of 2.73 Hz (Figure 4d). These frequency values exhibit a cyclical pattern with an approximate 24 h wavelength. The minima occur around 5:30 UTC, while the maxima are observed around 17:30 UTC each day. This pattern is particularly evident in the initial portion of the graph, spanning from the beginning of the recording until the start of October 22nd.

As for the distribution of HVSR values over time for P_1, these also exhibit notable variability (Figure 4e). The mean values of the HVSR average 5.75 over the entire period, with hourly values ranging from 4.24 to 8.07 units, representing a variability range of 3.83 units. The dispersion of values is relatively lower than that of the frequencies, as indicated by the dashed lines. Similar to what is observed in the P_1 frequencies, the temporal distribution of HVSR also displays a cyclical pattern, with a wavelength of approximately 24 h, reaching peaks around 7:30 UTC.

The frequency and HVSR curves displays an approximate half-period phase shift, indicating that the amplitude valleys align roughly with the frequency peaks, and vice versa. This phenomenon is evident in the scatter plot, where the linear regression line exhibits a negative slope and an R-squared coefficient of 0.5552, which is similar to what is observed with P_0 (Figure 4f).

For all charts, both the mean curve and its standard deviations follow a similar pattern, suggesting the reliability of the measurements.

5. Discussion

The evaluation of the HVSR calculation results for the acquired time record shows the presence of two well-defined peaks. These peaks are attributed to a stratigraphic origin, suggesting that P_0 is related to the contact between the sedimentary column and basement, while P_1 is associated with a shallower stratigraphic discontinuity. Currently, we cannot determine the interface responsible for P_1 due to the absence of subsurface Vs profiles in this area and the absence of distinct lithologic contrasts. To address this, future studies should prioritize investigating the distribution of Vs in the subsurface and correlating it with the geological record.

The results of the hourly analysis of the HVSR curves reveal limited variations for P_0, especially in terms of frequency, whereas substantial variations are observed for P_1, both in frequency and HVSR values. P_1 variations show a cyclical pattern of roughly 24 h. The relationship between frequency values and HVSR is inverse, with maximum frequency peaks coinciding with minimum HVSR values.

The amplitude of the HVSR peak has typically been attributed to the originating V_S contrast, with higher contrasts leading to higher amplitudes [63]. However, recent research indicates that other factors may affect the HVSR peak. In particular, V_S in a sedimentary body can be affected by fluctuations in water levels in its aquifer(s) and an increase in pore pressure, resulting in a decrease in effective stress and, consequently, a reduction in velocity. Several studies have linked the variation in wave propagation velocity to aquifer recharge [11,12,64–66].

To assess the possible influence of tides on changes in the shape of the HVSR, we compared our hourly records with water level data from the Río de la Plata for the same period (Figure 5). The hydrometric variations during the period studied are of the order of 1 m and reveal the semi-diurnal pattern characteristic of the Río de la Plata. The water-level data were smoothed using a moving window of 12 h to mitigate high-frequency variations. Similarly, the variations in the hourly HVSR analysis were also processed using a moving window of 12 h for comparative purposes.

The results show a certain correspondence between the cyclic behavior of the water level and that of the P_1 variations, both in terms of frequencies and HVSR amplitude values. In general, it was observed that an increase in frequency in the P_1 is roughly correlated with low estuarine levels, while a decrease in P_1 frequency is associated with higher water levels. As for the HVSR amplitude values of the peaks and the hydrometric curve, a direct correlation is observed.

Overall, the relationships between hydrometric variations and P_1 values, considering both frequency and HVSR amplitude, suggest that they are related to estuarine levels. Ambient noise variations do not have the same short period as semi-diurnal tidal variations, but their influence can be observed over longer periods, capturing the daily tidal cycles.

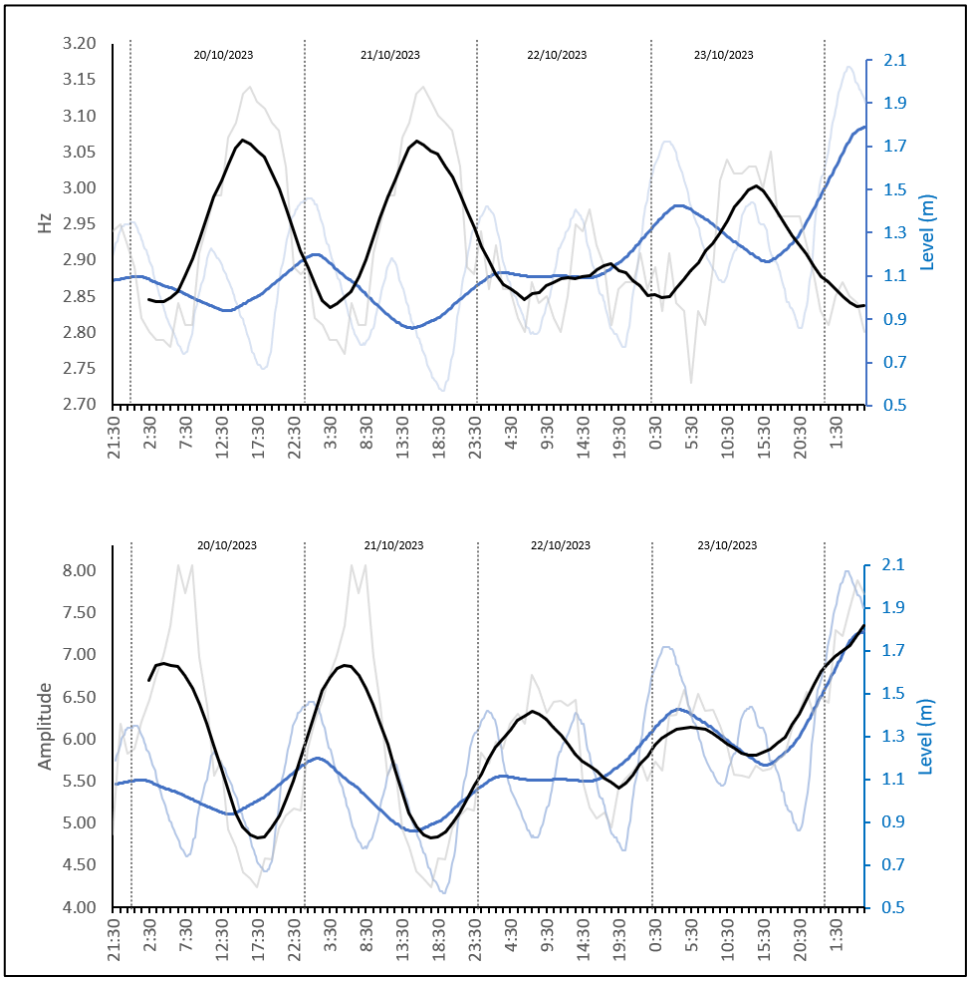

Figure 5. Comparison between HVSR P_1 frequency variations (**top**) and HVSR amplitude variations (**bottom**) with the level of the Río de la Plata. The light black lines represent the hourly records of the HVSR function, while the dark black lines represent the 12 h moving window. The light blue lines represent the variations of the Rio de la Plata, and the dark blue line represents the 12 h moving window level of the river.

To go further and visualize the possible effect of tides on the subsurface mechanical properties in the study area, we plotted temporal records from the unconfined aquifer and the semi-confined Puelche aquifer over five weeks between September and October 2015, located in the vicinity of the seismic station (Figure 1). Unfortunately, we lack contemporaneous records of tidal or ambient seismic noise, but the data reveal interesting observations (Figure 6).

Both aquifers show evident variations with periods close to one week. However, a more detailed analysis reveals a marked regularity in the high-frequency variations of the semi-confined aquifer, with a peak every six hours likely related to the semi-diurnal tidal effect of the Río de la Plata. These peaks are not present, at least evidently, in the unconfined aquifer. Previous studies have demonstrated a direct correlation between estuarine levels and increasing piezometric levels in the semi-confined Puelche aquifer [67,68]. Similarly, we attribute the high-frequency variations of the semi-confined aquifer to a mechanical effect, wherein loads resulting from tidal-related water-volume changes are transferred to piezometric levels [69,70]. This effect is not observed strongly in the phreatic aquifer, likely due to its unconfined nature.

Based on the aforementioned findings, and considering that our observations are restricted to a short period and are therefore limited, we hypothesize a possible conceptual model to explain the variations of the HVSR function over time.

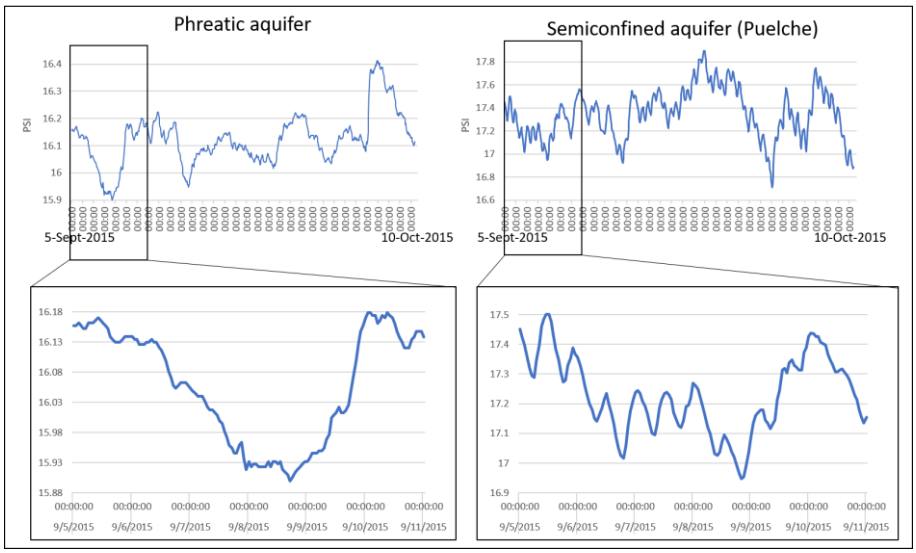

Figure 6. Measurements were obtained in 2015 for the unconfined aquifer and the semi-confined Puelche aquifer. Above are the data for the four weeks, and below is a detailed view of a six-day window. Values are given in pounds per square inch (PSI) units.

In general, we observe that during high tides, P_1 tends to exhibit relatively high amplitude values and relatively low frequency values, while during low tides, P_1 tends to exhibit relatively low amplitude values and relatively high frequency values. We believe that increases in the estuarine water level associated with the tidal regime are the source of higher ambient noise periods, translating into an increase in P_1 amplitudes during high tides. The increase of the HVSR peak amplitude with an increase of the noise intensity has been already documented in the literature (e.g., [34]).

Changes in estuarine hydrometric levels may also have additional effects on influencing the response of the HVSR function. At high tides, the unconfined aquifer levels rise and saturate more sediments, affecting their mechanical properties and decreasing the Vs. The changes in Vs produced by this effect would be subtle considering that the expected water table variations are in the order of centimeters. On the other hand, the rise in water volume in the estuary during high tides exerts an increased pressure on the estuarine bed. This pressure would propagate into the aquifer system, ultimately increasing the pore pressure inland, especially in the semi-confined aquifers (Figure 6). The increase in pore pressure counteracts the lithospheric pressure, resulting in a decrease in average Vs [39]. Given that the frequency of peaks in the HVSR spectrum is directly linked to the average Vs of the sedimentary column above the interface where the impedance contrast is generated [61], it is consistent to expect that a decrease in average Vs will be reflected in a reduction in peak frequency, and vice versa. Therefore, the relatively lower-frequency values of P1 observed during high tides can be attributed to a decrease in the average Vs of the sedimentary column promoted by an increase in the piezometric levels. Conversely, the relatively higher-frequency values of P1 during low tides are likely due to an increase in the average Vs of the sedimentary column (Figure 7).

The proposed conceptual model offers a plausible explanation for the anticipated variations in the HVSR function for peak P_1. It is based on experimental HVSR data, their relationship to hydrometric variations in the estuary, and pressure fluctuations in the aquifer system in response to tides. However, it is worth noting that the model assumptions have not been confirmed by direct measurements of Vs variations over time. The application of other types of analyses to ambient seismic noise records, such as the dv/v technique (e.g., [12]), could be crucial to validate these assumptions and improve the understanding of Vs dynamics with water level variations in the estuary. Furthermore, the limited resolution of our HVSR results at frequencies < 1 Hz prevents a comprehensive study of peak P_0

variations in time. More detailed investigations in this aspect would be beneficial to develop a more comprehensive model.

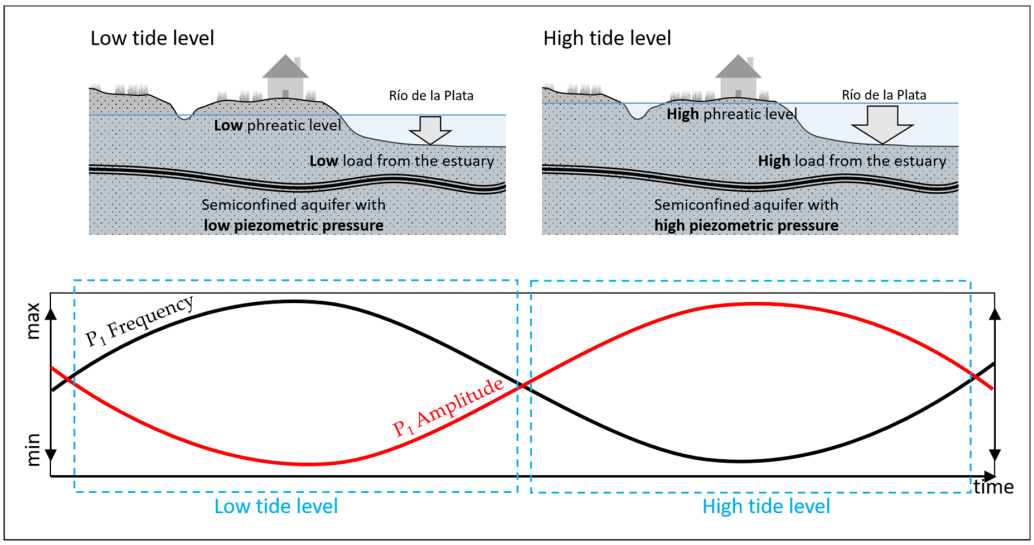

Figure 7. In the top panel, a conceptual model that relates variations in tides and loads and their effect in a multilayer aquifer. The triple black line represents a semi-permeable layer that separates the upper unconfined aquifer and the lower semiconfined aquifer (Puelche aquifer). The lower panel presents the schematic behavior of the HVSR amplitude and frequency as related to variations in tides.

6. Conclusions

The HVSR technique applied to ambient seismic noise has become relatively common in the literature in recent decades, owing to its versatility and relatively straightforward application. It is primarily used to determine the fundamental frequency of the soil and for geological studies aimed at estimating sediment thicknesses. Although HVSR peaks are usually considered stable, recent studies have shown temporal variations in both the amplitude and frequency of the peaks. Some studies attribute these variations to changes in the source of ambient seismic noise over time [32,34], while others find explanations in variations in subsurface properties [41,42]. The latter phenomenon may hold the greatest potential in the field of applied environmental seismology, as it opens up new possibilities for diverse monitoring applications.

In our study, we recorded and processed ambient seismic noise in the coastal plain of the Río de la Plata, Argentina, near a tide-influenced estuary. The HVSR function revealed two distinct peaks of stratigraphic origin, with P_0 interpreted as the interface between the basement and sediments, and P_1 interpreted as associated with a shallower discontinuity. Although the peaks generally persist throughout the record, we observed variations in frequency and amplitude, which are particularly pronounced in P_1. Temporal analysis of P_1 identified cyclic patterns that, when compared with estuarine levels, appear to indicate a relationship with tidal dynamics on approximately 24 h cycles.

We hypothesize that variations in the HVSR shape are multifactorial and are associated with (i) a change in the seismic noise source linked to Río de la Plata activity, that would play a pivotal role in the HVSR peak amplitude, (ii) changes in subsurface mechanical properties due to a slight rise in the water table, and (iii) changes in subsurface mechanical properties due to pore pressure variations in the aquifer system caused by differences in the estuarine water body load. Few works have taken tidal variations into account when studying their influence on HVSR curves [31,42]. This study provides new evidence on this aspect, highlighting its novelty by comparing HVSR curves with tidal variations on high-resolution time scales. Furthermore, these findings are discussed in terms of changes

in subsurface mechanical properties due to tidal action, trying to provide insight into the complex interactions involved.

Our results support the feasibility of ambient seismic noise as a promising tool for monitoring changes in aquifer levels, as well as for studying the dynamic relationship between aquifers and tides. Environmental seismology holds promise in hydrogeology, both in process studies and in monitoring applications, with the advantages of being non-invasive and cost-effective. Ongoing research aims to further explore these relationships for enhanced groundwater resource management, engaging professionals from both environmental seismology and hydrogeology.

Author Contributions: Conceptualization, L.G., F.P. and S.D.; software, L.G. and F.P.; validation, L.G., F.P. and S.D.; formal analysis, L.G., F.P. and S.D.; investigation, L.G., F.P. and S.D.; resources, S.D. and E.C. (Eleonora Carol); data curation, L.G. and F.P.; writing—original draft preparation, L.G., F.P. and S.D.; writing—review and editing, L.G., F.P., E.C. (Emanuele Colica), E.C. (Eleonora Carol), E.F., L.R., M.R.A., F.C. and S.D.; visualization, L.G.; supervision, F.P. and S.D.; project administration, S.D.; funding acquisition, L.G. and S.D. All authors have read and agreed to the published version of the manuscript.

Funding: This work has been supported by DEMUWA project (grant agreement number SRF2022-2S1) financed by the Malta Council for Science and Technology through the Space Research Fund (Building Capacity in the Downstream Earth Observation Sector), a program supported by the European Space Agency. Funds were also made available through the IPAS+ (Internationalisation Partnership Awards Scheme), funded by the Malta Council for Science and Technology.

Institutional Review Board Statement: Not applicable.

Informed Consent Statement: Not applicable.

Data Availability Statement: Data can be made available upon request.

Acknowledgments: The authors would like to extend their gratitude to Tomás Galone and Miguel A. Bignasco for their collaboration in data acquisition.

Conflicts of Interest: The authors declare no conflicts of interest. The funders had no role in the design of the study; in the collection, analyses, or interpretation of data; in the writing of the manuscript; or in the decision to publish the results.

References

1. Liu, Y.; Huang, X.; Yang, H. An Integrated Approach to Investigate the Coupling Coordination between Urbanization and Flood Disasters in China. *J. Clean. Prod.* **2022**, *375*, 134191. [CrossRef]
2. Malmir, M.; Javadi, S.; Moridi, A.; Randhir, T.; Saatsaz, M. Integrated Groundwater Management Using a Comprehensive Conceptual Framework. *J. Hydrol.* **2022**, *605*, 127363. [CrossRef]
3. Nistor, M.M.; Rahardjo, H.; Satyanaga, A.; Hao, K.Z.; Xiaosheng, Q.; Sham, A.W.L. Investigation of Groundwater Table Distribution Using Borehole Piezometer Data Interpolation: Case Study of Singapore. *Eng. Geol.* **2020**, *271*, 105590. [CrossRef]
4. Sendrós, A.; Urruela, A.; Himi, M.; Alonso, C.; Lovera, R.; Tapias, J.C.; Rivero, L.; Garcia-Artigas, R.; Casas, A. Characterization of a Shallow Coastal Aquifer in the Framework of a Subsurface Storage and Soil Aquifer Treatment Project Using Electrical Resistivity Tomography (Port de La Selva, Spain). *Appl. Sci.* **2021**, *11*, 2448. [CrossRef]
5. Zhang, Z.; Weiping, W. Managing Aquifer Recharge with Multi-Source Water to Realize Sustainable Management of Groundwater Resources in Jinan, China. *Environ. Sci. Pollut. Res.* **2021**, *28*, 10872–10888. [CrossRef]
6. Stehly, L.; Fry, B.; Campillo, M.; Shapiro, N.M.; Guilbert, J.; Boschi, L.; Giardini, D. Tomography of the Alpine Region from Observations of Seismic Ambient Noise. *Geophys. J. Int.* **2009**, *178*, 338–350. [CrossRef]
7. Gu, N.; Gao, J.; Wang, B.; Lu, R.; Liu, B.; Xu, X.; Zhang, H. Ambient Noise Tomography of Local Shallow Structure of the Southern Segment of Tanlu Fault Zone at Suqian, Eastern China. *Tectonophysics* **2022**, *825*, 229234. [CrossRef]
8. Scolaro, S.; Pino, P.; D'Amico, S.; Orecchio, B.; Presti, D.; Torre, A.; Totaro, C.; Farrugia, D.; Neri, G. Ambient Noise Measurements for Preliminary Microzoning Studies in the City of Messina, Sicily. *Ann. Geophys.* **2018**, *61*, 4. [CrossRef]
9. Panzera, F.; Tortorici, G.; Romagnoli, G.; Marletta, G.; Catalano, S. Empirical Evidence of Orthogonal Relationship between Directional Site Effects and Fracture Azimuths in an Active Fault Zone: The Case of the Mt. Etna Lower Eastern Flank. *Eng. Geol.* **2020**, *279*, 105900. [CrossRef]
10. Panzera, F.; Alber, J.; Imperatori, W.; Bergamo, P.; Fäh, D. Reconstructing a 3D Model from Geophysical Data for Local Amplification Modelling: The Study Case of the Upper Rhone Valley, Switzerland. *Soil Dyn. Earthq. Eng.* **2022**, *155*, 107163. [CrossRef]

11. Rodríguez Tribaldos, V.; Ajo-Franklin, J.B. Aquifer Monitoring Using Ambient Seismic Noise Recorded with Distributed Acoustic Sensing (DAS) Deployed on Dark Fiber. *J. Geophys. Res. Solid Earth* **2021**, *126*, e2020JB021004. [CrossRef]
12. Laudi, L.; Agius, M.R.; Galea, P.; D'Amico, S.; Schimmel, M. Monitoring of Groundwater in a Limestone Island Aquifer Using Ambient Seismic Noise. *Water* **2023**, *15*, 2523. [CrossRef]
13. Barrière, J.; Krein, A.; Oth, A.; Schenkluhn, R. An Advanced Signal Processing Technique for Deriving Grain Size Information of Bedload Transport from Impact Plate Vibration Measurements. *Earth Surf. Process. Landf.* **2015**, *40*, 913–924. [CrossRef]
14. Geay, T.; Belleudy, P.; Gervaise, C.; Habersack, H.; Aigner, J.; Kreisler, A.; Seitz, H.; Laronne, J.B. Passive Acoustic Monitoring of Bed Load Discharge in a Large Gravel Bed River. *J. Geophys. Res. Earth Surf.* **2017**, *122*, 528–545. [CrossRef]
15. Eibl, E.P.S.; Bean, C.J.; Einarsson, B.; Pàlsson, F.; Vogfjörd, K.S. Seismic Ground Vibrations Give Advanced Early-Warning of Subglacial Floods. *Nat. Commun.* **2020**, *11*, 2504. [CrossRef] [PubMed]
16. Preiswerk, L.E.; Walter, F. High-Frequency (>2 Hz) Ambient Seismic Noise on High-Melt Glaciers: Green's Function Estimation and Source Characterization. *J. Geophys. Res. Earth Surf.* **2018**, *123*, 1667–1681. [CrossRef]
17. Burjánek, J.; Gassner-Stamm, G.; Poggi, V.; Moore, J.R.; Fäh, D. Ambient Vibration Analysis of an Unstable Mountain Slope. *Geophys. J. Int.* **2010**, *180*, 820–828. [CrossRef]
18. Galea, P.; D'Amico, S.; Farrugia, D. Dynamic Characteristics of an Active Coastal Spreading Area Using Ambient Noise Measurements—Anchor Bay, Malta. *Geophys. J. Int.* **2014**, *199*, 1166–1175. [CrossRef]
19. Panzera, F.; D'Amico, S.; Lotteri, A.; Galea, P.; Lombardo, G. Seismic Site Response of Unstable Steep Slope Using Noise Measurements: The Case Study of Xemxija Bay Area, Malta. *Nat. Hazards Earth Syst. Sci.* **2012**, *12*, 3421–3431. [CrossRef]
20. Borzì, A.M.; Minio, V.; Cannavò, F.; Cavallaro, A.; D'Amico, S.; Gauci, A.; De Plaen, R.; Lecocq, T.; Nardone, G.; Orasi, A.; et al. Monitoring Extreme Meteo-Marine Events in the Mediterranean Area Using the Microseism (Medicane Apollo Case Study). *Sci. Rep.* **2022**, *12*, 21363. [CrossRef]
21. Gerstoft, P.; Fehler, M.C.; Sabra, K.G. When Katrina Hit California. *Geophys. Res. Lett.* **2006**, *33*, L17308. [CrossRef]
22. Nakamura, Y. A method for dynamic characteristics estimation of subsurface using microtremor on the ground surface. *Railw. Tech. Res. Inst. Q. Rep.* **1989**, *30*, 25–33.
23. Nogoshi, M. On the Amplitude Characteristics of Microtremor, Part II. *J. Seismol. Soc. Jpn.* **1971**, *24*, 26–40.
24. Cara, F.; Cultrera, G.; Azzara, R.M.; De Rubeis, V.; Di Giulio, G.; Giammarinaro, M.S.; Tosi, P.; Vallone, P.; Rovelli, A. Microtremor Measurements in the City of Palermo, Italy: Analysis of the Correlation between Local Geology and Damage. *Bull. Seismol. Soc. Am.* **2008**, *98*, 1354–1372. [CrossRef]
25. Mucciarelli, M.; Gallipoli, M. A Critical Review of 10 Years of Microtremor HVSR Technique. *Boll. Geofis. Teor. Appl.* **2001**, *42*, 255–266.
26. Panou, A.A.; Theodulidis, N.; Hatzidimitriou, P.; Stylianidis, K.; Papazachos, C.B. Ambient Noise Horizontal-to-Vertical Spectral Ratio in Site Effects Estimation and Correlation with Seismic Damage Distribution in Urban Environment: The Case of the City of Thessaloniki (Northern Greece). *Soil Dyn. Earthq. Eng.* **2005**, *25*, 261–274. [CrossRef]
27. Panzera, F.; Bergamo, P.; Fäh, D. Canonical Correlation Analysis Based on Site-Response Proxies to Predict Site-Specific Amplification Functions in Switzerland. *Bull. Seismol. Soc. Am.* **2021**, *111*, 1905–1920. [CrossRef]
28. Theodoulidis, N.; Cultrera, G.; De Rubeis, V.; Cara, F.; Panou, A.; Pagani, M.; Teves-Costa, P. Correlation between Damage Distribution and Ambient Noise H/V Spectral Ratio: The SESAME Project Results. *Bull. Earthq. Eng.* **2008**, *6*, 109–140. [CrossRef]
29. Bonnefoy-Claudet, S.; Cornou, C.; Bard, P.-Y.; Cotton, F.; Moczo, P.; Kristek, J.; Fäh, D. H/V Ratio: A Tool for Site Effects Evaluation. Results from 1-D Noise Simulations. *Geophys. J. Int.* **2006**, *167*, 827–837. [CrossRef]
30. Hobiger, M.; Bard, P.-Y.; Cornou, C.; Le Bihan, N. Single Station Determination of Rayleigh Wave Ellipticity by Using the Random Decrement Technique (RayDec). *Geophys. Res. Lett.* **2009**, *36*, L14303. [CrossRef]
31. Becker, D.; Cristiano, L.; Peikert, J.; Kruse, T.; Dethof, F.; Hadziioannou, C.; Meier, T. Temporal Modulation of the Local Microseism in the North Sea. *J. Geophys. Res. Solid Earth* **2020**, *125*, e2020JB019770. [CrossRef]
32. Benkaci, N.; Oubaiche, E.H.; Chatelain, J.-L.; Bensalem, R.; Benouar, D.; Abbes, K. Non-Stability and Non-Reproducibility of Ambient Vibration HVSR Peaks in Algiers (Algeria). *J. Earthq. Eng.* **2021**, *25*, 853–871. [CrossRef]
33. La Rocca, M.; Chiappetta, G.D.; Gervasi, A.; Festa, R.L. Non-Stability of the Noise HVSR at Sites near or on Topographic Heights. *Geophys. J. Int.* **2020**, *222*, 2162–2171. [CrossRef]
34. La Rocca, M.; Chiappetta, G.D. Day–Night Cycle of Seismic Noise HVSR and Comparison with Body Waves and T Waves. *Geophys. J. Int.* **2022**, *231*, 1535–1544. [CrossRef]
35. Lontsi, A.M.; Hobiger, M.; Panzera, F.; Sánchez-Sesma, F.J.; Fäh, D. Seismic Characterization of Swiss Strong-Motion Borehole-Station Sites by Inversion of Full Microtremor Horizontal-to-Vertical Spectral Ratios [H/V(z, f)]. *Bull. Seismol. Soc. Am.* **2023**, *113*, 417–436. [CrossRef]
36. Amalokwu, K.; Best, A.I.; Sothcott, J.; Chapman, M.; Minshull, T.; Li, X.-Y. Water Saturation Effects on Elastic Wave Attenuation in Porous Rocks with Aligned Fractures. *Geophys. J. Int.* **2014**, *197*, 943–947. [CrossRef]
37. D'Hour, V.; Schimmel, M.; Do Nascimento, A.F.; Ferreira, J.M.; Lima Neto, H.C. Detection of Subtle Hydromechanical Medium Changes Caused By a Small-Magnitude Earthquake Swarm in NE Brazil. *Pure Appl. Geophys.* **2016**, *173*, 1097–1113. [CrossRef]
38. Bergamo, P.; Donohue, S.; Gunn, D.A.; Dashwood, B.; Uhlemann, S.; Chambers, J.E.; Ward, D. *Time-Lapse Monitoring of the Slopes of a Heritage Earthwork by Means of Near-Surface Seismic Techniques*; European Association of Geoscientists & Engineers: Utrecht, The Netherlands, 2015; Volume 2015, pp. 1–5.

39. Yu, H.; Hilterman, F.J. Shear Wave Sensitivity to Pore Pressure Prediction. In *SEG Technical Program Expanded Abstracts 2013*; SEG Technical Program Expanded Abstracts; Society of Exploration Geophysicists: Houston, TX, USA, 2013; pp. 600–604.
40. Kula, D.; Olszewska, D.; Dobiński, W.; Glazer, M. Horizontal-to-Vertical Spectral Ratio Variability in the Presence of Permafrost. *Geophys. J. Int.* **2018**, *214*, 219–231. [CrossRef]
41. Rigo, A.; Sokos, E.; Lefils, V.; Briole, P. Seasonal Variations in Amplitudes and Resonance Frequencies of the HVSR Amplification Peaks Linked to Groundwater. *Geophys. J. Int.* **2021**, *226*, 1–13. [CrossRef]
42. Seivane, H.; García-Jerez, A.; Navarro, M.; Molina, L.; Navarro-Martínez, F. On the Use of the Microtremor HVSR for Tracking Velocity Changes: A Case Study in Campo de Dalías Basin (SE Spain). *Geophys. J. Int.* **2022**, *230*, 542–564. [CrossRef]
43. Mianzan, H.; Lasta, C.; Acha, E.; Guerrero, R.; Macchi, G.; Bremec, C. The Río de La Plata Estuary, Argentina-Uruguay. In *Coastal Marine Ecosystems of Latin America*; Ecological Studies; Seeliger, U., Kjerfve, B., Eds.; Springer: Berlin/Heidelberg, Germany, 2001; pp. 185–204, ISBN 978-3-662-04482-7.
44. Framiñan, M.B.; Etala, M.P.; Acha, E.M.; Guerrero, R.A.; Lasta, C.A.; Brown, O.B. Physical Characteristics and Processes of the Río de La Plata Estuary. In *Estuaries of South America: Their Geomorphology and Dynamics*; Environmental Science; Perillo, G.M.E., Piccolo, M.C., Pino-Quivira, M., Eds.; Springer: Berlin/Heidelberg, Germany, 1999; pp. 161–194, ISBN 978-3-642-60131-6.
45. Guerrero, R.A.; Acha, E.M.; Framinan, M.B.; Lasta, C.A. Physical Oceanography of the Río de La Plata Estuary, Argentina. *Cont. Shelf Res.* **1997**, *17*, 727–742. [CrossRef]
46. Cavallotto, J.L. Evolución Geomorfológica de la Llanura Costera Ubicada en el Margen sur del Río de la Plata. Ph.D. Thesis, Universidad Nacional de La Plata (UNLP), La Plata, Argentina, 1995.
47. Fidalgo, F.; Martinez, O. Algunas Características Geomorfológicas Dentro Del Partido de La Plata, Provincia de Buenos Aires. *Rev. Asoc. Geológica Argent.* **1983**, *38*, 263–279.
48. Fidalgo, F.; Colado, U.R.; De Francesco, F.O. Sobre ingresiones marinas cuaternarias en los partidos de casteli, chacomus y magdalena (pcia. de buenos aires). *Buenos Aires Dep. Argent. Sci. Publ.* **1973**, *3*, 227–240.
49. Fucks, E.E.; D'Amico, G.; Pisano, M.F.; Nuccetelli, G. Evolución geomorfológica de la región del Gran La Plata y su relación con eventos catastróficos. *Rev. Asoc. Geológica Argent.* **2017**, *74*, 141–154.
50. Santucci, L.; Carol, E.; Borzi, G.; García, M.G. Hydrogeochemical and Isotopic Signature of Surface and Groundwater in a Highly Industrialized Sector of the Rio de La Plata Coastal Plain (Argentina). *Mar. Pollut. Bull.* **2017**, *120*, 387–395. [CrossRef]
51. Kruse, E.E.; Carol, E.S.; Mancuso, M.; Laurencena, P.C.; Deluchi, M.H.; Rojo, A. Recharge Assessment in an Urban Area: A Case Study of La Plata, Argentina. *Hydrogeol. J.* **2013**, *21*, 1091–1100. [CrossRef]
52. Logan, W.S.; Nicholson, R.V. Origin of Dissolved Groundwater Sulphate in Coastal Plain Sediments of the Rio de La Plata, Eastern Argentina. *Aquat. Geochem.* **1997**, *3*, 305–328. [CrossRef]
53. Carol, E.; Kruse, E.; Tejada, M. Surface Water and Groundwater Response to the Tide in Coastal Wetlands: Assessment of a Marsh in the Outer Río de La Plata Estuary, Argentina. *J. Coast. Res.* **2013**, *165*, 1098–1103. [CrossRef]
54. Santucci, L.; Romina, S.; Eleonora, C.; Esteban, V.; Héctor, P. Using H, O, Rn Isotopes and Hydrometric Parameters to Assess the Surface Water-Groundwater Interaction in Coastal Wetlands Associated to the Marginal Forest of the Río de La Plata. *Cont. Shelf Res.* **2019**, *186*, 104–110. [CrossRef]
55. Wathelet, M.; Chatelain, J.; Cornou, C.; Giulio, G.D.; Guillier, B.; Ohrnberger, M.; Savvaidis, A. Geopsy: A User-Friendly Open-Source Tool Set for Ambient Vibration Processing. *Seismol. Res. Lett.* **2020**, *91*, 1878–1889. [CrossRef]
56. Leucci, G.; Persico, R.; De Giorgi, L.; Lazzari, M.; Colica, E.; Martino, S.; Iannucci, R.; Galone, L.; D'Amico, S. Stability Assessment and Geomorphological Evolution of Sea Natural Arches by Geophysical Measurement: The Case Study of Wied Il-Mielah Window (Gozo, Malta). *Sustainability* **2021**, *13*, 12538. [CrossRef]
57. Vella, A.; Galea, P.; D'Amico, S. Site Frequency Response Characterisation of the Maltese Islands Based on Ambient Noise H/V Ratios. *Eng. Geol.* **2013**, *163*, 89–100. [CrossRef]
58. Konno, K.; Ohmachi, T. Ground-Motion Characteristics Estimated from Spectral Ratio between Horizontal and Vertical Components of Microtremor. *Bull. Seismol. Soc. Am.* **1998**, *88*, 228–241. [CrossRef]
59. Chandler, V.W.; Lively, R.S. Utility of the Horizontal-to-Vertical Spectral Ratio Passive Seismic Method for Estimating Thickness of Quaternary Sediments in Minnesota and Adjacent Parts of Wisconsin. *Interpretation* **2016**, *4*, SH71–SH90. [CrossRef]
60. Galone, L.; D'Amico, S.; Colica, E.; Iregbeyen, P.; Galea, P.; Rivero, L.; Villani, F. Assessing Shallow Soft Deposits through Near-Surface Geophysics and UAV-SfM: Application in Pocket Beaches Environments. *Remote Sens.* **2024**, *16*, 40. [CrossRef]
61. Molnar, S.; Cassidy, J.F.; Castellaro, S.; Cornou, C.; Crow, H.; Hunter, J.A.; Matsushima, S.; Sánchez-Sesma, F.J.; Yong, A. Application of Microtremor Horizontal-to-Vertical Spectral Ratio (MHVSR) Analysis for Site Characterization: State of the Art. *Surv. Geophys.* **2018**, *39*, 613–631. [CrossRef]
62. Galone, L.; Colica, E.; D'Amico, S.; Cellone, F.; Carol, E.; Fucks, E.E. Progresses in European Earthquake Engineering and Seismology. In Proceedings of the Third European Conference on Earthquake Engineering and Seismology, Bucharest, Romania, 4–9 September 2022; pp. 4596–4600.
63. Oubaiche, E.H.; Chatelain, J.-L.; Bouguern, A.; Bensalem, R.; Machane, D.; Hellel, M.; Khaldaoui, F.; Guillier, B. Experimental Relationship between Ambient Vibration H/V Peak Amplitude and Shear-Wave Velocity Contrast. *Seismol. Res. Lett.* **2012**, *83*, 1038–1046. [CrossRef]
64. Clements, T.; Denolle, M.A. Tracking Groundwater Levels Using the Ambient Seismic Field. *Geophys. Res. Lett.* **2018**, *45*, 6459–6465. [CrossRef]

65. Kim, D.; Lekic, V. Groundwater Variations From Autocorrelation and Receiver Functions. *Geophys. Res. Lett.* **2019**, *46*, 13722–13729. [CrossRef]
66. Lecocq, T.; Longuevergne, L.; Pedersen, H.A.; Brenguier, F.; Stammler, K. Monitoring Ground Water Storage at Mesoscale Using Seismic Noise: 30 Years of Continuous Observation and Thermo-Elastic and Hydrological Modeling. *Sci. Rep.* **2017**, *7*, 14241. [CrossRef]
67. Alcaraz, M.; Carrera, J.; Cuello, J.E.; Guarracino, L.; Vives, L. Determining Hydraulic Connectivity of the Coastal Aquifer System of La Plata River Estuary (Argentina) to the Ocean by Analysis of Aquifer Response to Low-Frequency Tidal Components. *Hydrogeol. J.* **2021**, *29*, 1587–1599. [CrossRef]
68. Cuello, J.E.; Guarracino, L.; García Alcaraz, M.d.M.; Vives, L.S.; Carrera, J. Mechanical interaction between the Río de La Plata and the coastal aquifer system in the Northeast of the Province of Buenos Aires, Argentina. *Boletín Geológico Min.* **2022**, *133*, 227–243. [CrossRef]
69. Guarracino, L.; Carrera, J.; Vázquez-Suñé, E. Analytical Study of Hydraulic and Mechanical Effects on Tide-Induced Head Fluctuation in a Coastal Aquifer System That Extends under the Sea. *J. Hydrol.* **2012**, *450–451*, 150–158. [CrossRef]
70. Monachesi, L.B.; Guarracino, L. Exact and Approximate Analytical Solutions of Groundwater Response to Tidal Fluctuations in a Theoretical Inhomogeneous Coastal Confined Aquifer. *Hydrogeol. J.* **2011**, *19*, 1443–1449. [CrossRef]